Journal of Materials Chemistry C

PAPER

View Article Online
View Journal | View Issue

Cite this: J. Mater. Chem. C, 2019, 7, 3037

Insights into the local structure of dopants, doping efficiency, and luminescence properties of lanthanide-doped $CsPbCl_3$ perovskite nanocrystals†

Ju-Ping Ma,[a] Ya-Meng Chen,[a] Lu-Min Zhang,[a] Shao-Qiang Guo,[b] Jian-Dang Liu,[c] Hong Li,[a] Bang-Jiao Ye,[c] Zhi-Yong Li,[a] Yang Zhou,[ad] Bin-Bin Zhang,[a] Osman M. Bakr,[d] Jun-Ying Zhang *[b] and Hong-Tao Sun *[ae]

Doping has been established as a powerful approach for endowing lead halide perovskite nanocrystals (NCs) with novel properties. However, our fundamental understanding of the local structure of dopants, doping efficiency and luminescence properties of these NCs is still very sparse. Here, we provide the first experimental evidence regarding the local structure of rare earth ions in $CsPbCl_3$ NCs, based on the analysis of extended X-ray absorption fine structure spectroscopy. Our result suggests that Yb^{3+} occupies the Pb^{2+} crystallographic sites in $CsPbCl_3$ NCs. We further demonstrate a strategy to examine the determinant of the doping efficiency in lanthanide-doped lead halide perovskite NCs, which enables us to uncover the important role of structural defects in affecting the doping efficiency. A broad range of experimental characterization techniques including steady-state and time-resolved luminescence spectra, X-ray absorption spectra, and positron annihilation lifetime spectra, coupled with first-principles calculations, help us identify that the doping efficiency is associated with structural defects in NCs and that the formation of a higher-concentration of defects favors incorporation of a higher-concentration of dopants into the lattice. Importantly, we demonstrate that the concept of defect-assisted doping is not limited to the model system of Yb^{3+}-doped $CsPbCl_3$ NCs, but can be used as a guideline to rationally tune the doping efficiency of lanthanide-doped halide perovskite NCs. We also show that lanthanide-doped $CsPbCl_3$ NCs demonstrate anomalous decay of the band-edge emission, which we propose is due to the existence of shallow trapping states near the conduction band. Our results greatly deepen the understanding of the structural and photophysical properties of lanthanide-doped lead halide perovskite NCs, and highlight the possibility to use the chemistry of defects to tailor the doping efficiency of halide perovskite NCs.

Received 13th January 2019,
Accepted 8th February 2019

DOI: 10.1039/c9tc00237e

rsc.li/materials-c

Introduction

Lead halide perovskite nanocrystals (NCs) are an emerging family of low-cost, solution-processable semiconducting materials, which have attracted a great deal of interest for applications in a diverse range of high-performance optoelectronic devices such as solar cells, lasers, and light-emitting diodes (LEDs).[1–16] Similar to their bulk counterparts,[17,18] one common strategy used for tailoring the properties of lead halide perovskite NCs is based on compositional engineering, which can be readily achieved by mixing halide ions or cations in the precursors or by post-synthesis ion exchange under mild reaction conditions, which allows very fine control over the NCs' band gap.[19–22]

Recently, it has been recognized that the targeted introduction of heteroatoms into halide perovskites can work as an additional lever, beyond structural perfection and compositional distinction, for endowing lead halide perovskites with many

[a] College of Chemistry, Chemical Engineering and Materials Science, Soochow University, Suzhou 215123, China. E-mail: timothyhsun@gmail.com
[b] Department of Physics, Beihang University, Beijing 100191, China. E-mail: zjy@buaa.edu.cn
[c] State Key Laboratory of Particle Detection and Electronics, Department of Modern Physics, University of Science and Technology of China, Hefei, Anhui 230026, P. R. China
[d] Division of Physical Sciences and Engineering, King Abdullah University of Science and Technology (KAUST), Thuwal 23955-6900, Saudi Arabia
[e] State Key Laboratory of Luminescence and Applications, Changchun Institute of Optics, Fine Mechanics and Physics, Chinese Academy of Sciences, Changchun 130033, China

† Electronic supplementary information (ESI) available: Additional synthesis methods, the model used for the DFT calculations, XRD, TEM, and other supplementary data. See DOI: 10.1039/c9tc00237e

novel properties.[23–50] This approach was first employed for tuning the electronic and optical properties of lead halide perovskite films and single crystals,[24,25] and then extended to tailor the properties of their nano-sized relatives.[26–39,45,46] So far, a wide range of metal ions, including Bi^{3+},[35] transition metal ions (*e.g.*, Mn^{2+} and Ni^{2+}),[27–34] and rare earth ions,[36,38–44] have been doped into matrices of lead halide perovskite NCs, which introduces a series of novel functionalities including new emission bands, an improved photoluminescence quantum yield (PLQY), or enhanced stability.[23] Rare-earth doped lead halide perovskite NCs have received particular attention because of the extremely expanded luminescence properties.[36–38] However, until now, there is no direct structural evidence that explains the incorporation of rare earth ions into the lattice of halide perovskite NCs, and the occupied crystallographic sites of rare earth ions in the lattice thus remain unknown.

Various parameters such as the reaction temperature and duration, the precursors used, the stoichiometry of the reactants, the chemical potentials of the constituent atoms, and the surface morphology and shape of the NCs could impact doping of foreign ions into the lattice of NCs.[34,51] Practically, correlating these factors with the doping efficiency remains a grand challenge, and design strategies for establishing such a link remain largely obscure, because of the difficulty in decoupling one factor from all possible sources. Additionally, it is well recognized that lead halide perovskite NCs commonly possess structural defects such as atomic vacancies.[1,23,34] Nevertheless, to date, it remains unknown whether the doping efficiency is associated with structural defects formed during growth of NCs. Understanding the determinants affecting the doping efficiency thus merits detailed studies to rationally control the doping and to obtain more doped perovskite NCs with alluring properties.

Here, for the first time, we experimentally examine the local structure of rare earth ions in doped $CsPbCl_3$ NCs based on the analysis of extended X-ray absorption fine structure (EXAFS) spectra. Our result clearly evidences that Yb^{3+} substitutes for Pb^{2+}. On this basis, we further provide a strategy to investigate the determinant of the doping efficiency in lead halide perovskite NCs, which enables us to uncover the important role of structural defects in affecting the doping efficiency. The key for the strategy's success lies in unchanging all factors related to the synthesis by using a one-pot method that yields separable doped NCs with diverse sizes and crystal qualities, thus allowing us to give a detailed study of the doping efficiency and the structure of separated NCs. We first chose Yb^{3+}-doped $CsPbCl_3$ NCs as an example system.[36–38] Interestingly, we find that larger NCs show an obviously higher doping efficiency than their smaller cousins, although they are from the same synthesis batch. Detailed structural and photophysical characterization including EXAFS, positron annihilation spectroscopy, and optical spectroscopy, combined with density functional theory (DFT) calculations, leads us to establish a clear correlation between doping efficiency and structural defects in NCs. We find that a higher density of structural defects in larger NCs formed during growth favors incorporation of a larger concentration of dopants into the lattice. Importantly, we find that the concept of defect-assisted doping can be used as a guideline to rationally control the doping efficiency of lanthanide-doped halide perovskite NCs. Interestingly, we also discover that lanthnide-doped halide perovskite NCs can demonstrate anomalous decay and thermal quenching behavior of the band-edge emission, which we attribute to the existence of shallow defect levels near the conduction band.

Experimental section

Materials and chemicals

All chemicals, cesium carbonate (Cs_2CO_3, 99.99%, Aladdin), lead(II) chloride ($PbCl_2$, 99.999%, Alfa Aesar), ytterbium chloride ($YbCl_3$, 99.99%, Alfa Aesar), lanthanum chloride ($LaCl_3$, 99.99%, Alfa Aesar), lead(II) acetate trihydrate ($Pb(Ac)_2{\cdot}3H_2O$, 99.999%, Acros), poly(methyl methacrylate) (PMMA, average $M_w \sim 350\,000$ by GPC, Aldrich), 1-octadecene (ODE, 90%, Alfa Aesar), oleic acid (OA, 90%, Alfa Aesar), oleylamine (OAm, 80–90%, Acros), tri-*n*-octylphosphine (TOP, 90%, Alfa Aesar), benzoyl chloride (99%, Sigma-Aldrich), methyl acetate (MA, 99%, Alfa Aesar), *n*-hexane (Hex, $\geq$98.0% (GC), Aladdin) and toluene (AR, QS), were used without purification unless otherwise noted.

Preparation of Cs-oleate

In a typical procedure, a mixture of 0.4073 g Cs_2CO_3, 1.35 mL OA and 15 mL ODE was added to a 50 mL 3-neck round-bottomed flask and degassed at 120 °C under a vacuum for 1 h. Then the mixture was heated to 150 °C under N_2 until all Cs_2CO_3 was dissolved. The solution was kept at 150 °C.

Synthesis of Yb-doped $CsPbCl_3$ NCs for the X-ray absorption measurement

$PbCl_2$ (0.2644 g), $YbCl_3$ (0.2656 g), ODE (20 mL), OAm (3.2 mL), OA (3.2 mL), and TOP (4 mL) were added into a 50 mL three-neck round-bottomed flask, degassed at 120 °C for 1 h, and then heated at 120 °C under N_2. Then, 3.2 mL of dried OAm and 3.2 mL of dried OA were slowly injected into the solution. Ten minutes later, the temperature was raised to 220 °C and kept at 220 °C for 5 min. Finally, the Cs-oleate (1.8 mL, 0.15 M in ODE) was quickly injected and 1 min later the reaction mixture was cooled down by an ice-water bath. To purify the NCs, the crude solution was separated by centrifuging for 5 min at 12 000 rpm using a desktop high-speed centrifuge (H1650-W, Cence). After centrifugation, the supernatant was discarded and this process was repeated two more times to remove the residual reaction mixture. Then the precipitate was redispersed in 0.75 mL hexane and 0.75 mL MA and centrifuged again for 5 min at 12 000 rpm, and the supernatant was discarded. Subsequently, the particles were redispersed in 1.5 mL hexane and centrifuged for 5 min at 12 000 rpm, and the supernatant was discarded. After repeating the previous step, the final samples were obtained. Note that this method can get NCs with uniform sizes. The obtained NCs were denoted $CsPbCl_3$:Yb NCs.

Synthesis of Yb-doped $CsPbCl_3$ NCs with a wide size distribution

$PbCl_2$ (0.1521 g), $YbCl_3$ (0.1527 g), ODE (10 mL), OAm (1.6 mL), OA (1.6 mL), and TOP (2 mL) were added into a 50 mL 3-neck round-bottomed flask, degassed at 120 °C for 1 h, and then heated at 120 °C under N_2. After that, 1.6 mL of dried OAm and 1.6 mL of dried OA were slowly injected into the above mixture. Ten minutes later, the temperature was raised to 240 °C. Then, 0.8 mL of dried OAm and 0.8 mL of dried OA were subsequently injected into the reaction mixture and it was kept at 240 °C for 5 min. Finally, the Cs-oleate (1.035 mL, 0.15 M in ODE) was quickly injected and 1 min later the reaction mixture was cooled down by an ice-water bath. Note that OA and OAm were degassed at 100 °C for 2 h under a vacuum, which were defined as dried OA and dried OAm, respectively. After centrifugation, the supernatant was discarded and this process was repeated two more times to remove the residual reaction mixture. Then the precipitate was redispersed in 0.75 mL hexane and 0.75 mL MA and centrifuged again for 5 min at 12 000 rpm, and the supernatant was discarded. We note that the obtained NCs feature a wide size distribution, as shown below. Subsequently, we used a multi-centrifugation method to separate the NCs.[52] The particles were redispersed in 1.5 mL hexane and centrifuged for 5 min at 12 000 rpm, and the supernatant was reserved and denoted S-Yb-1. After repeating the previous step three more times, different NC sets were collected, which are denoted S-Yb-2, S-Yb-3, and S-Yb-4, respectively. The methods for the synthesis of other samples are shown in the ESI.†

Composition, structure and TEM characterization

X-ray diffraction (XRD) patterns were taken with an X'Pert-Pro MPD diffractometer (Netherlands PANalytical) with a Cu Kα X-ray source (λ = 1.540598 Å). The samples for XRD measurements were evaporated, redispersed in toluene again, and then dropped on a glass substrate. These steps were all done at room temperature. Inductively coupled plasma mass spectrometry (ICP-MS) (iCAPTM Qc, Thermo Scientific) was used to determine the concentration of lead and ytterbium or lanthanum ions. Transmission electron microscopy (TEM) images were collected on an FEI Tecnai G20 S-TWIN TMP microscope operated at 200 kV. Samples were prepared by drying ~10 μL of dilute NC solution in hexane/toluene on a carbon-coated copper grid.

Positron annihilation lifetime spectroscopy measurements

The positron annihilation lifetime spectra were taken by using an ORTEC fast-fast coincidence system with a time resolution of ~200 ps (full-width at half-maximum) at room temperature. A 20 μCi ^{22}Na positron source was sandwiched between two identical samples, and the total counts of each lifetime spectrum exceeded 3 million. Positron lifetime spectra were deconvoluted by using the LT9 code. One channel represents the time of 12.7 ps. The average lifetime is calculated by the following equation,

$$\tau_m = \sum_{i=1}^{k+1} I_i \tau_i \quad (1)$$

where τ_m is the average lifetime, τ_i corresponds to different positron lifetimes, and I_i corresponds to the relative intensity.

Absorption and luminescence measurements

The absorption spectra were collected with a double-beam UV-vis-NIR spectrophotometer (Cary 5000, Agilent). Steady-state photoluminescence (PL) spectra for S-Yb-*x* were measured using a 375 nm laser as the excitation source. The signal was analyzed by a single-grating monochromator and detected by a liquid-nitrogen-cooled CCD detector. The spectral response of the detection system was corrected by a standard optical source (DH-3-BAL-CAL-EXT, Ocean Optics). Temperature-dependent PL spectra for S-La-*x* thin films were obtained by exciting the sample with a 375 nm semiconductor laser. The films were mounted in a helium exchange cryostat and the PL was analyzed using a monochromator (Horiba, iHR550) and detected using an electrically cooled PMT (Hamamatsu, R928). In order to prevent the agglomeration of NCs, the polymer (PMMA) is introduced before the preparation. PMMA powder was dissolved in toluene at a concentration of 25 mg mL^{-1}. The NC solution was evaporated, redispersed in PMMA/toluene again at a concentration of 1 g mL^{-1}, and spin-coated (700 rpm, 30 s) onto a quartz substrate. The copolymer composite films were kept in a nitrogen atmosphere for further measurements. The PL spectra of other samples were collected on a spectrometer equipped with a 450 W xenon lamp (FLS980, Edinburgh Instruments). Room-temperature PLQYs were measured using an integration sphere incorporated into a spectrofluorometer (FluoroLog, Horiba) equipped with a 450 W xenon lamp. Time-resolved PL measurements of visible luminescence were acquired on a Lifespec II setup (Edinburgh Instruments, UK) using a picosecond-pulsed 373 nm laser (pulse width: 43 ps) as the excitation source. The excitation energy density is 4.0 μJ cm^{-2}. Time-resolved PL measurements of Yb luminescence were performed by detecting the modulated luminescence signal with a photomultiplier tube (Hamamatsu, H10330-75) and then analyzing the signal with a photon-counting multichannel scaler; the samples were pumped by 355 nm light from a Nd-YAG laser system with a repetition frequency of 10 Hz. All NC solutions were diluted to an optical density of *ca.* 0.08 at the corresponding excitation wavelength.

X-ray absorption spectroscopy

The X-ray absorption spectra of the Pb L_{III}-edge and Yb L_{III}-edge for the Yb-doped $CsPbCl_3$ NC samples were obtained on the 1W2B beam line of the Beijing Synchrotron Radiation Facility with a stored electron energy of 2.5 GeV and average ring currents of 200 mA. A fixed-exit Si(111) double crystal monochromator was used. The NCs were repeatedly synthesized according to the synthesis methods described above to obtain sufficient amounts of NCs for the measurement of the X-ray absorption spectra. The obtained NCs were evenly dispersed on single-sided adhesive tape (Scotch). Data were collected in transmission mode at room temperature. The Pb (Alfa Aesar, 99.9%) and $PbCl_2$ (Alfa Aesar, 99.999%) powders, Yb (Aladdin, 99.9%) and Yb_2O_3 (Aladdin, 99.99%) were used as reference

samples. The oxide layer for the Pb powder was removed by annealing at 150 °C for 1 h under a reducing atmosphere (H_2/N_2: 5%). All X-ray absorption spectra were taken at room temperature. The obtained data were analyzed using the IFEFFIT software package.

Density functional theory (DFT) calculations

We mainly considered point defects in pure (undoped) and doped $CsPbCl_3$, namely, atomic vacancies (V_{Cl}, V_{Pb}, and V_{Cs} in pure $CsPbCl_3$ and Yb-V_{Cl}, Yb-V_{Pb}, and Yb-V_{Cs} in doped $CsPbCl_3$) and substitutional defects (Yb_{Pb}). All calculations were performed using the Vienna ab initio simulation package (VASP) based on DFT using projector augmented wave (PAW) potentials.[53,54] A single point at the generalized gradient approximation (GGA) of Perdew–Burke–Ernzerhof (PBE) was employed to treat the exchange–correlation energy. The cutoff energy of the plane-wave basis was set to 450 eV. The self-consistent total-energy difference and the convergence criterion for forces on atoms were set to 10^{-4} eV and 0.01 eV $Å^{-1}$, respectively. For first Brillouin zone integration, we selected a 3 × 3 × 3 Monkhorst–Pack mesh for a 3 × 3 × 3 supercell. Fig. S1 (ESI†) shows the position of the Yb dopant, Cl vacancy, Cs vacancy and Pb vacancy, respectively. After the introduction of the vacancy and dopant, all the systems were fully relaxed. The number of atoms and lattice parameters ($a = b = c$, and volume, V) in the 3 × 3 × 3 $CsPbCl_3$ supercell before and after introducing the vacancy/dopant are listed in Table S1 (ESI†). The lattice parameters of a relaxed cell for pure $CsPbCl_3$ are found to be $a = b = c = 5.721$ Å, in good agreement with other theoretical results (5.7285 Å).[55] A small difference exists between the experimental values ($a = b = c = 5.605$ Å) and the calculated results. The total electric charges of the systems containing a vacancy/dopant are set to 0 e (*i.e.*, the systems are electrically neutral). The valence states of the atoms around the vacancy/dopant were obtained by subtracting the core charge from the calculated Bader charge as listed in Table S1 (ESI†). Because of the large supercell and great number of atoms, all calculations of band structures and densities of states (DOSs) were performed based on the PBE functional. In both band structures and DOSs, the zero energy point was set to the Fermi level of the pure $CsPbCl_3$. The system with a defect was corrected by aligning the average electrostatic potential of Cs atoms located far from the defect to that of the same element in the pure $CsPbCl_3$.

Results and discussion

Local structure of Yb^{3+} ions in $CsPbCl_3$ NCs

We chose Yb^{3+}-doped $CsPbCl_3$ NCs as a model system to investigate the local structure of Yb^{3+} ions in the $CsPbCl_3$ lattice. The reason for choosing Yb^{3+} ions as dopants lies in the fact that Cs and Pb have strong X-ray absorption capabilities. Compared with other lighter lanthanide ions, the fluorescence signal from the Yb element is relatively less influenced by Cs and Pb when taking the X-ray absorption spectra in fluorescence mode, a method generally used when the dopant concentration is not high. We found that even for the Yb element, its concentration should be high to obtain the Yb L_{III}-edge EXAFS spectrum with a good signal to noise ratio. The Yb^{3+}-doped $CsPbCl_3$ NCs used for the X-ray absorption spectrum have a Yb to Pb molar ratio of 2.71% and an average edge length of 9.17 nm (Fig. S2, ESI†). The powder XRD pattern indicates that these NCs adopt a cubic phase of space group $Pm\bar{3}m$ (221) (Fig. S3, ESI†).

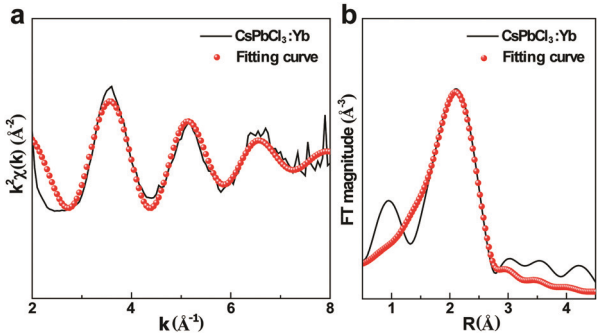

Fig. 1 (a) k^2-Weighted Yb L_{III}-edge EXAFS and (b) corresponding FT of $CsPbCl_3$:Yb NCs.

Fig. 1 shows the Yb L_{III}-edge EXAFS spectrum and the corresponding Fourier transform (FT) for the Yb^{3+}-doped $CsPbCl_3$ NCs. As is well recognized, the peak in R space corresponds to the interatomic distances between absorbing and surrounding atoms.[34] Because of photoelectron phase shift, the peak position in the FT can decrease by *ca.* 0.5 Å relative to the actual interatomic distance. It is noted that there is a peak at about 2.07 Å (the distance not phase corrected) in R space (Fig. 1b), which is only slightly smaller than the bond length of Pb–Cl in $CsPbCl_3$ but much smaller than that of the Cs–Cl bond length, after considering the photoelectron phase shift (Fig. S4, ESI†). This strongly suggests that the Yb^{3+} ions most possibly substitute for the Pb^{2+} ions instead of the Cs^+ ions. To examine this possibility, we then analyzed the obtained EXAFS spectrum through a single-shell fit over an R range of 1.35–4.0 Å by the IFEFFIT software package.[56] We used the model of Yb^{3+} ions at the Pb^{2+} sites in $CsPbCl_3$ for this analysis, which was constructed *ab initio* using the FEFF program code in the IFEFFIT software package. Five parameters were used for the fitting: the coordination number (CN), the energy shift (ΔE_0), the adjustment of the half path length (ΔR), the mean-square relative displacement of absorber and backscatter atoms (σ^2), and the correction to the imaginary energy (E_i). As displayed in Fig. 1b, the spectrum can be fitted well, with CN = 4.50 ± 0.42, $\Delta E_0 = -23.04 \pm 1.84$ eV, $\Delta R = 0.022 \pm 0.021$ Å, $\sigma^2 = 0.021 \pm 0.002$ $Å^2$, and $E_i = -4.70 \pm 1.09$ eV. All these facts indicate that the incorporated Yb^{3+} ions are at the Pb^{2+} sites. To the best of our knowledge, this represents the first structural evidence that indicates the occupied crystallographic sites of rare earth ions in the lead halide perovskite lattice.

Doping efficiency and optical properties of lanthanide-doped $CsPbCl_3$ NCs

We next investigated the doping efficiency and optical properties of lanthanide-doped $CsPbCl_3$ NCs. Here, we synthesized Yb^{3+}-doped $CsPbCl_3$ NCs by a modified approach (see the

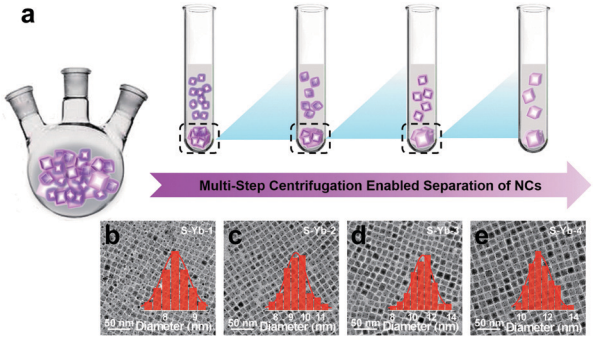

Fig. 2 (a) Schematic illustration of the strategy for attainment of NCs with different sizes and qualities. (b–e) TEM image of S-Yb-1 (b), S-Yb-2 (c), S-Yb-3 (d), and S-Yb-4 (e). The insets of (b–e) show the histograms of edge lengths of NCs. The average sizes and standard deviations for S-Yb-1, S-Yb-2, S-Yb-3 and S-Yb-4 are 8.35 ± 0.02 nm, 9.33 ± 0.06 nm, 11.07 ± 0.07 nm, and 11.35 ± 0.07 nm, respectively. Note that the average sizes are obtained by Gaussian fitting.

synthesis details in the Experimental section),[1,36,38] which allowed us to obtain NCs with a wide size distribution (Fig. S5, ESI†). Such as-prepared NCs were then subjected to multi-step, high-speed centrifugation using hexane as the solvent, which allows us to separate these NCs into diverse fractions with different average sizes (Fig. 2a). The fractions were denoted S-Yb-*x*, where *x* represents the centrifugation number of times (CNT) of NCs dispersed in 1.5 mL hexane. We find that the size of S-Yb-*x* is notably different. With the increase of the CNT, the edge length of NCs gradually increases, from 8.35 nm for S-Yb-1 to 11.35 nm for S-Yb-4 (Fig. 2b–e). We note that the product yield decreases as the CNT increases (Table S2, ESI†), and that all obtained products are phase-pure as confirmed by powder XRD (Fig. S6, ESI†).

The method used here relies on multi-centrifugation to separate the NCs, which involves the use of hexane to disperse the NCs. Considering that the increase of the CNT means that NCs interact with more hexane, we devised the following experiment to examine the influence of hexane on the properties of the NCs by monitoring the change of the PL of the NCs. Using S-Yb-1 as the model case, we diluted three S-Yb-1 solutions with *n*-hexane and adjusted the optical density to 1, 2, and 3. This means that each NC interacts with different amounts of hexane. After keeping the solutions for two hours, we diluted them to an identical optical density of 0.08 at 375 nm, and then measured the PL. The samples were denoted OD1, OD2, and OD3, according to the original optical density. We find that all these samples demonstrate almost identical PL with respect to S-Yb-1 (Fig. S7, ESI†), suggesting that the use of more hexane cannot notably affect the quality of NCs.

Another possible source that can affect the NCs' quality is the centrifugation process, because it may be argued that the centrifugal force could strip off the organic capping agents of NCs that can result in the introduction of defects on the NCs' surface. We then devised the following method to examine this possibility. We diluted three S-Yb-1 solutions with *n*-hexane and adjusted the optical density to 1, 2, and 3. These NC solutions were centrifuged for 5 min at 12 000 rpm. This process is repeated three times in order to maintain consistency with the sample preparation process. Finally, all NC solutions were diluted to an optical density of 0.08 at 375 nm to compare the PL intensity. These solutions were denoted OD1-C, OD2-C, and OD3-C, according to the original optical density. As shown in Fig. S8 (ESI†), we can see that the PL intensity almost does not change, indicating that the centrifugation process cannot affect the NCs' quality. We speculate that the most possible reason is that the NCs were capped by a large number of organic agents, given the fact that all S-Yb-*x* NCs are heavily oily.

Beyond the expectation that all as-synthesized NCs have the same doping efficiency, the most interesting thing we find is that the concentration of Yb^{3+} ions notably rises with the increase of the CNT, from a Yb/Pb molar ratio of 0.62% in S-Yb-1 to 1.21% in S-Yb-4 (Table S2, ESI†). This gives a direct indication that more dopants can be incorporated into larger NCs. After Yb^{3+} doping, the PLQYs of S-Yb-1, S-Yb-2, S-Yb-3, and S-Yb-4 are 87.9%, 80.6%, 67.0%, and 58.3%, respectively, much larger than that of their undoped counterpart (Fig. S9, ESI†).[1,34] The absorption edge and band-edge emission of doped NCs slightly redshift with the increase of the NCs' size (Fig. 3a and b), which probably results from size-induced minor alteration of the absorbing and emitting states in NCs.[57,58] We point out that recent detailed structural analysis suggests that all-inorganic lead halide perovskite NCs were composed of ordered subdomains that are hinged through a two-/three-dimensional network of twin boundaries.[59] We surmise that doping of Yb^{3+} into the lattice may affect the subdomains of NCs, which

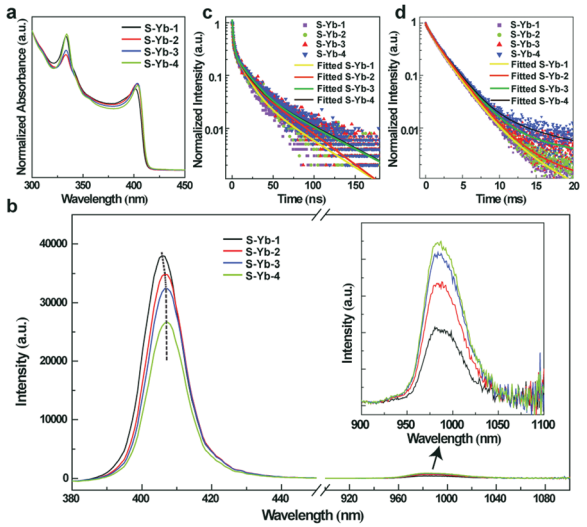

Fig. 3 (a) Absorption spectra of S-Yb-*x*. (b) Visible emission (left) and near-infrared (NIR) emission spectra of S-Yb-*x*. The inset shows the enlarged NIR emission spectra. The dotted line shows the change of the emission peak. The FWHMs of visible PL for S-Yb-1, S-Yb-2, S-Yb-3 and S-Yb-4 are 13.1 nm, 13.0 nm, 12.9 nm and 12.8 nm, respectively. Note that the visible and NIR emission spectra were taken by the same detection system, the spectral response of which was corrected by a standard optical source. (c) Time-resolved PL of S-Yb-*x*; the monitored wavelength is 407 nm. (d) Time-resolved PL of Yb^{3+} emission in S-Yb-*x*; the monitored wavelength is 980 nm.

probably affect the absorbing and emitting states. Broad emission bands centered at 980 nm from the separated NC sets are observed (Fig. 3b), which can be ascribed to the characteristic emission of Yb^{3+} ions that were excited by energy transfer from excitons of $CsPbCl_3$ NCs to Yb^{3+} ions.[36,38] As a result, the lifetimes of band-edge emission of $CsPbCl_3$ NCs are expected to be shortened from S-Yb-1 to S-Yb-4 because of the increased concentration of Yb^{3+} ions. Furthermore, the decreased PLQYs of the band-edge emission hint that the corresponding lifetimes should be shortened from S-Yb-1 to S-Yb-4, if the energy transfer from the excitons to the Yb^{3+} ions is the only energy loss channel for the band-edge emission. However, it is very interesting that the corresponding lifetime of the band-edge emission from S-Yb-1 to S-Yb-4 increases anomalously (Fig. 3c and Table S3, ESI†). This strongly evidences that other energy relaxation channels contribute to the decay process, which will be discussed below. As shown in Fig. 3d, the PL kinetics at 980 nm becomes slower upon Yb doping from 0.62% to 1.21%, resulting in increased average lifetimes (Table S4, ESI†).

We reasoned that the obtained NC sets with different sizes from the same synthesis batch should feature different crystal qualities, because of different growth rates. Given that the crystal quality is intimately associated with the local coordination environments of the constituent atoms and that EXAFS spectroscopy is a powerful technique for the examination of the local coordination environment and local order around the absorbing atoms,[34,60,61] we therefore took the EXAFS spectra at the Pb L_{III}-edge for the representative samples S-Yb-1 and S-Yb-4. The k^2-weighted Pb L_{III}-edge EXAFS and the corresponding Fourier transforms (FTs) of S-Yb-1 and S-Yb-4 are shown in Fig. 4a and b. We note that the magnitude of S-Yb-1 in R space is slightly stronger than that of S-Yb-4 (Fig. 4b), signifying the slightly better structural order around Pb atoms in S-Yb-1. To gain further insight into the difference in crystal quality for S-Yb-1 and S-Yb-4, we then carried out a single-shell fit of both EXAFS spectra. Four parameters were used for the fitting: CN, ΔE_0, ΔR, and σ^2. As shown in Fig. 4a and b and Table 1, although S-Yb-1 and S-Yb-4 have comparable σ^2 values (0.0151 Å^2 for S-Yb-1 and 0.0154 Å^2 for S-Yb-4), the coordination number of Pb with chloride atoms in S-Yb-4 is slightly smaller than that in S-Yb-1. Based on the fact that the EXAFS analysis typically gives an uncertainty of ±20% in the determination of the CN,[61] the EXAFS result, to a small extent, suggests that larger $CsPbCl_3$ NCs with higher Yb concentrations probably exhibit a relatively poorer structural order compared with their smaller cousins with low Yb concentrations. We note that recent work on Mn doped halide perovskite NCs revealed a doping concentration-dependent bond length using X-ray absorption fine structure measurements.[62] However, owing to the low concentration of Yb ions in the doped NCs, the change of bond length is not so significant (Table 1).

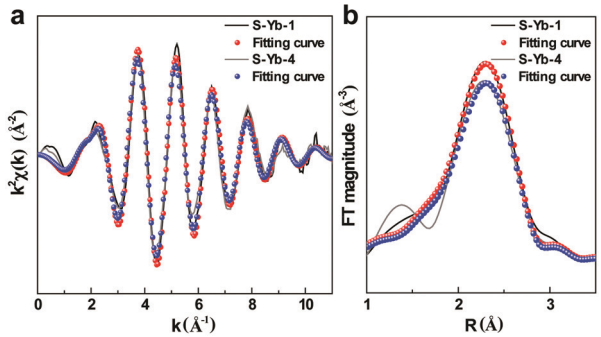

Fig. 4 (a) k^2-Weighted Pb L_{III}-edge EXAFS and (b) corresponding FTs of S-Yb-1 and S-Yb-4.

The small difference in the short-range order of Pb^{2+} ions in Yb^{3+}-doped NCs with different sizes stimulates us to seek a more sensitive measurement technique to explain their difference. Positron annihilation lifetime spectrometry is a well established sensitive technique to examine defects in solids, and measuring the lifetime of positrons can provide information about the type and relative concentration of defects at the sub-nm scale, even at the parts-per-million level. The general working principle is based on correlating the lifetime (dwell time) of the injected positrons with the sample void (or vacancy) size (longer lifetimes correspond to large void sizes).[63–65] By monitoring the evolution of the positron lifetimes in the targeted systems, one can glean important clues regarding the changes in the types and relative concentrations of defects.[63–65]

As shown in Fig. 5, the positron lifetime spectra of both S-Yb-1 and S-Yb-4 yield three lifetime components (Table 2). The longest component (τ_3, 2.43 ns for S-Yb-1 and 2.74 ns for S-Yb-4) could be associated with large-size defects, probably subdomain boundaries in NCs, because it was revealed that the $CsPbCl_3$ NCs are composed of multiple subdomains.[59] The shortest lifetime can be tentatively assigned to atomic vacancies, such as Cl, Cs or Pb vacancies, whereas τ_2 probably is associated with a large vacancy complex, probably connected with Yb dopants. We note that the average positron lifetime in S-Yb-4 is longer than that in S-Yb-1, suggesting a higher concentration of defects in S-Yb-4. Interestingly, it is found that, in comparison with S-Yb-1, S-Yb-4 possesses a shorter τ_2 with a smaller percent (20.71%) and a longer τ_3 with a larger

Table 1 Main fitting results of the fit performed on the Pb L_{III}-edge k^2-weighted EXAFS spectra for S-Yb-1 and S-Yb-4

Sample	Shell	CN[a]	ΔE_0[b] (eV)	σ^2[c] (Å^2)	R[d] (Å)	R-Factor
S-Yb-1	Pb–Cl	5.47 ± 0.34	−0.75 ± 0.60	0.0151 ± 0.0010	2.83 ± 0.01	0.0044
S-Yb-4	Pb–Cl	5.14 ± 0.57	−1.06 ± 1.05	0.0154 ± 0.0017	2.84 ± 0.01	0.0205

[a] The fitted coordination number. [b] The energy shift. [c] The mean-square relative displacement of absorber and backscatter atoms. [d] Distance between absorber and backscatter atoms; R is the effective distance used in the model plus ΔR.

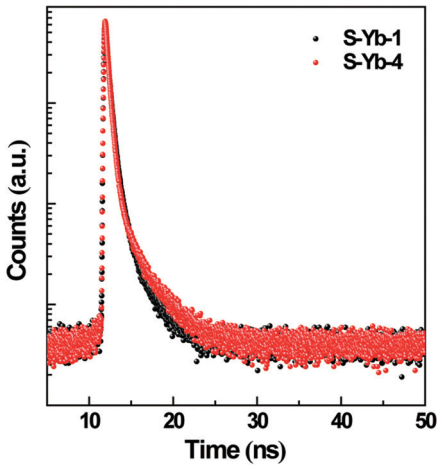

Fig. 5 Positron lifetime spectra of S-Yb-1 and S-Yb-4.

Table 2 Positron lifetime parameters of S-Yb-1 and S-Yb-4

Sample	τ_1 (ns)	τ_2 (ns)	τ_3 (ns)	I_1 (%)	I_2 (%)	I_3 (%)	τ_m (ns)
S-Yb-1	0.28	0.68	2.43	58.77	34.37	6.87	0.57
S-Yb-4	0.29	0.61	2.74	69.68	20.71	9.61	0.59

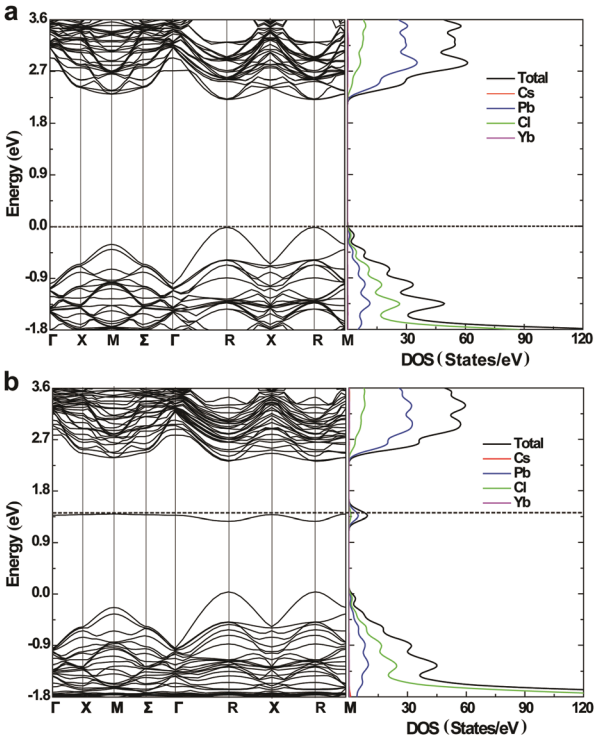

Fig. 6 (a) Band structure and DOS of Yb-doped $CsPbCl_3$ with a Cs vacancy. (b) Band structure and DOS of Yb-doped $CsPbCl_3$ with a Cl vacancy. The dotted lines in (a and b) represent the Fermi levels.

percent (9.61%). This suggests that the relative concentration of different defects is different in both samples, and S-Yb-4 has a higher concentration of large-size defects. We surmise that this may be triggered by the increase of the defect concentration in NCs. Collectively, this analysis clearly evidences that S-Yb-4 possesses a higher-concentration of structural defects.

To gain insight into the impact of atomic vacancies on the electronic structure and DOSs of Yb^{3+}-doped $CsPbCl_3$ NCs, we next performed DFT calculations.[60,61] We consider four models for doped $CsPbCl_3$, featuring Yb^{3+}-doped $CsPbCl_3$ without any defects and Yb^{3+}-doped $CsPbCl_3$ with Cl, Cs and Pb vacancies. We note that, similar to undoped $CsPbCl_3$,[34] the states around the band gap for doped $CsPbCl_3$ mainly come from Pb and Cl atoms, whereas Cs and Yb have no contribution. It is noted that, although Cl, Cs and Pb vacancies cannot notably affect the electronic band structure of doped $CsPbCl_3$ (Fig. 6 and Fig. S10, ESI†), the introduction of Cl vacancies can give rise to deep defect levels that function as nonradiative recombination channels (Fig. 6b), which may be one reason for the decreased total emission intensity in larger Yb^{3+}-doped NCs. We note that there are other possibilities for the existence of other types of large-size defects, as suggested by positron annihilation lifetime spectroscopy, which possibly introduce shallow defect levels near the conduction band.

Based on all experimental and theoretical results, we establish that larger Yb^{3+}-doped $CsPbCl_3$ NCs possess high-concentration defects and Yb ions, *i.e.*, the doping efficiency can be associated with structural defects in NCs. We are thus intrigued whether this phenomenon also exist in other lanthanide-doped halide perovskite systems. For this purpose, we grew La^{3+}-doped $CsPbCl_3$ NCs and then separated these NCs to get sets with different sizes. All of the obtained products are phase-pure as confirmed by powder XRD (Fig. S11, ESI†) (see the synthesis details in the ESI†). One reason for choosing La^{3+} as the dopant is that the ionic radius of La^{3+} is much larger than that of Yb^{3+} (six-coordinate ionic radii are 103 and 87 pm for La^{3+} and Yb^{3+}, respectively),[66] which can lead us to examine whether the observed phenomenon also exists for large-size dopants. Another benefit lies in the optical inactivity of La^{3+}, which makes it easier to gain deep insight into the photophysical properties. The samples were denoted S-La-*x*, where *x* represents the CNT of NCs dispersed in 1 mL hexane. Interestingly, we find a similar phenomenon as observed in Yb^{3+}-doped $CsPbCl_3$ NCs. With the increase of the CNT, the edge length of NCs notably increases, from 8.0 nm for S-La-1 to 15.4 nm for S-La-3. Correspondingly, the La concentration increases from 2.28% for S-La-1 to 6.60% for S-La-3 (Fig. 7a–c). Additionally, we find that the size increase of NCs causes a redshift of absorption and emission bands (Fig. 7d and e). Notably, the band-edge emission becomes weaker from S-La-1 to S-La-3, when all PL spectra were measured under the same optical density of NC solutions. Given the fact that La^{3+} is optically inactive, we conclude that larger La^{3+}-doped NCs have higher-concentration structural defects that introduce more nonradiative recombination channels. Therefore, this result offers additional evidence that the doping efficiency is related to structural defects.

We further investigated the PL decay kinetics of the band-edge emission in La^{3+}-doped $CsPbCl_3$ NCs. Interestingly, as shown in Fig. 8a and Table S5 (ESI†), the lifetime increases from S-La-1 to S-La-3, which is in marked contrast with the

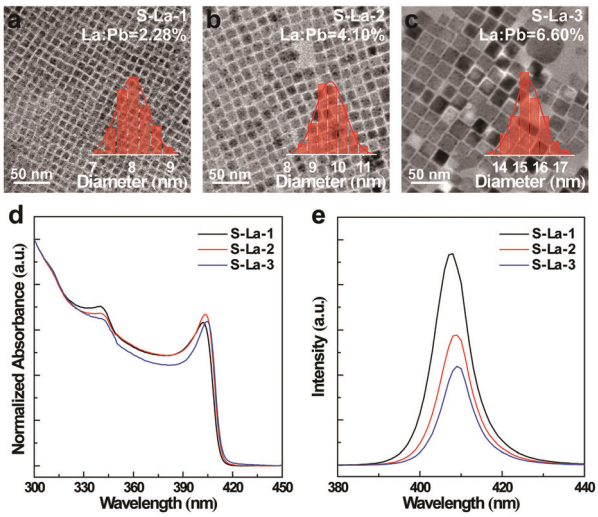

Fig. 7 (a–c) TEM image of S-La-1 (a), S-La-2 (b), and S-La-3 (c). The La concentrations are indicated in the TEM images. The insets show the histograms of edge lengths of NCs. The average sizes and standard deviations for S-La-1, S-La-2, and S-La-3 are 8.02 ± 0.02 nm, 9.70 ± 0.03 nm, and 15.41 ± 0.06 nm, respectively. Note that the average sizes are obtained by Gaussian fitting. (d and e) Absorption (d) and PL (e) spectra of S-La-1, S-La-2, and S-La-3. The FWHMs of PL for S-La-1, S-La-2, and S-La-3 are 10.8 nm, 10.3 nm, and 9.9 nm, respectively. The excitation wavelength for PL is 375 nm, and all PL spectra were measured under the same optical density of NC solutions.

steady-state PL results, but is similar to the trend as observed in Yb^{3+}-doped NCs. Based on this fact, we can conclude that other pathways are involved in the decay process. As carrier trapping is a thermally activated process, we next investigated the temperature-dependent PL of La^{3+}-doped $CsPbCl_3$ NCs dispersed in PMMA. The PL intensity of S-La-1 monotonously decreases with an increase of temperature from 250 K to 315 K, suggesting the enhanced trapping of photogenerated charge carriers at high temperatures. Interestingly, it is found that the PL intensity of S-La-3 decreases from 250 K to 296 K, but increases from 296 K to 302 K, and then decreases when further increasing the temperature (Fig. 8b). The observation of negative thermal quenching in a narrow temperature range is interesting. In recent work by Samanta *et al.*, negative thermal quenching of luminescence is also observed in a broader temperature range for Cd^{2+}-doped $CsPbCl_3$ NCs.[67] Two types of trapping centers can affect the PL behavior. One is a deep trapping center (*e.g.*, Cl vacancies in $CsPbCl_3$) that causes nonradiative recombination. This type of center is detrimental to the PL emission, resulting in a decreased PLQY and a shortened lifetime. The other is a shallow trap center, which lies very close to the excitonic state. The trapping–detrapping process related to this type of center is temperature dependent, and the charge carriers trapped in these shallow trap states can return to the excitonic state at moderate temperatures by thermal energy and recombine radiatively. This type of center results in an increased PL intensity and lifetime, when the trapped carriers can be thermally liberated.[67]

In our experiment, with the increase of the dopant concentration, the room-temperature decay dynamics of the band-edge

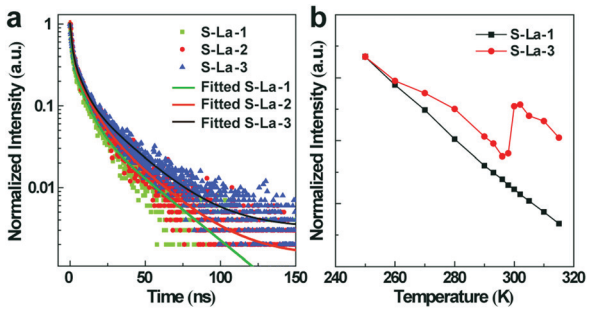

Fig. 8 (a) Time-resolved PL of S-La-*x*; the monitored-wavelength is 407 nm. (b) Variation of the PL intensity of S-La-1 and S-La-3 with temperature in the range of 250–315 K.

emission for both Yb^{3+}- and La^{3+}-doped NCs becomes slower, suggesting a similar intrinsic mechanism for this phenomenon. The combined experimental and theoretical results lead us to propose the following plausible model for the observed PL behavior. In the smaller NCs with a low-concentration of dopants, the concentration of shallow trapping states is limited, and the deep trapping state dominates the PL behavior, which demonstrates normal thermal quenching of the band-edge emission (Fig. 9a). However, in the larger NCs with a high-concentration of dopants, both deep and shallow trapping centers affect the PL behavior; in a moderate temperature range, the trapped charge carriers at shallow trapping centers near the conduction band will contribute to the lengthening of PL lifetimes (Fig. 9b). We point out that the extent to which the lifetime is lengthened is intimately associated with the concentration of shallow traps and the release rate of trapped carriers from these traps. As is experimentally revealed, the larger NCs with a higher concentration of dopants have a higher-density of structural defects (Fig. 4, 5 and 7), which provides chances for the introduction of a higher-concentration of shallow trapping states that can cause the increased lifetimes of the band-edge

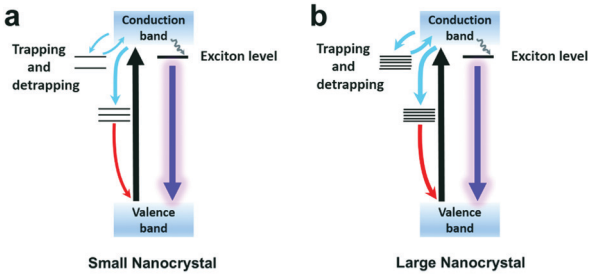

Fig. 9 Schematic illustration of the mechanism of PL properties for small (a) and larger (b) NCs with low- and high-concentration defects, respectively. The pale curved line represents the nonradiative relaxation from the conduction band to the exciton level. The black and violet arrow lines represent the excitation and band-edge emission, respectively. The blue arrow lines represent the trapping or detrapping of charge carriers. The thickness of the blue arrow line indicates the degree of trapping or detrapping of charge carriers. The red arrow lines represent the nonradiative recombination of trapped electrons with photogenerated holes. The thickness of the red arrow line indicates the degree of nonradiative recombination of trapped electrons with photogenerated holes.

emission (Fig. 3c and 8a). Therefore, the longer lifetime of the band-edge emission in larger NCs in the series of S-Yb-*x* and S-La-*x* can be viewed as a reflection of the increased concentration of structural defects. Specifically, for Yb^{3+}-doped NCs, the nonradiative energy transfer from the excitons to Yb^{3+} ions results in the NIR emission at 980 nm. We stress that the occurrence of the shallow defect levels near the conduction band probably plays a role in this energy transfer process. As recently revealed by Gamelin and coworkers, ultrafast optical spectroscopy measurements hint that the incorporation of rare-earth ions into the $CsPbCl_3$ NCs introduces a shallow defect level possibly caused by a defect complex.[38]

As is well recognized, the coordination of Yb^{3+} ions with organic capping agents generally results in strong quenching of NIR emission.[56] However, the Yb^{3+} emission in our samples is long-lived (Fig. 3d), comparable to that in inorganic matrices, suggesting that most of the Yb^{3+} ions are internally doped.[36–38] This is in good agreement with the EXAFS result. We note that, although larger Yb^{3+}-doped NCs are more defective than their smaller cousins, the average lifetimes of Yb^{3+} emission in larger NCs are longer than those in smaller ones (Fig. 3d), probably because more dopants are in the bulk in larger NCs (*i.e.*, with less Yb^{3+} at or near the surface of NCs). We point out that previous results show that the NIR emission characteristics of Yb^{3+}-doped $CsPbCl_3$ NCs are closely related to the synthesis methods used,[36,38,47] which may be due to the difference in defect types and concentration and the Yb distribution in these NCs. Based on our results and previous work,[36,38,47] synthesizing Yb^{3+}-doped $CsPbCl_3$ NCs that have defects and a Yb distribution suitable for Yb emission is the key to realize efficient NIR emission. We stress that at present the exact distribution of dopants in halide perovskites (*e.g.*, the ratio of dopants at or near the surface to those in the bulk and the homogeneity of dopants) is not clear, which remains an open question for further research.[23]

Generality of defect-assisted doping

Our results suggest a new view of doping: that dopants are most easily introduced into NCs with higher-concentration structural defects. We thus term this finding as a concept of defect-assisted doping. Interestingly, we find that this finding is also applicable to Yb^{3+}-doped $CsPb(Cl,Br)_3$ NCs (Fig. S12, ESI†). We next test the possibility of using this concept as a guideline to intentionally control the doping efficiency of lanthanide-doped halide perovskite NCs. As previously revealed, under Cl-poor conditions, the formation energies of atomic vacancies are much lower than those under Cl-rich conditions.[34] We thus synthesized Yb^{3+}-doped $CsPbCl_3$ NCs under Cl-poor conditions by merely decreasing the amount of the Cl source while maintaining all other factors unchanged. The powder XRD patterns confirm that the products are phase-pure (Fig. S13, ESI†) (see the synthesis details in the ESI†). Interestingly, we find that the Yb^{3+} concentration in NCs synthesized under Cl-poor conditions is much larger than that under Cl-rich conditions, although they have a similar size (Fig. S14, ESI†). We stress that this finding is in the framework of lanthanide-doped lead halide perovskite NCs, and whether it is applicable to other classes of doped NCs deserves to be further studied.

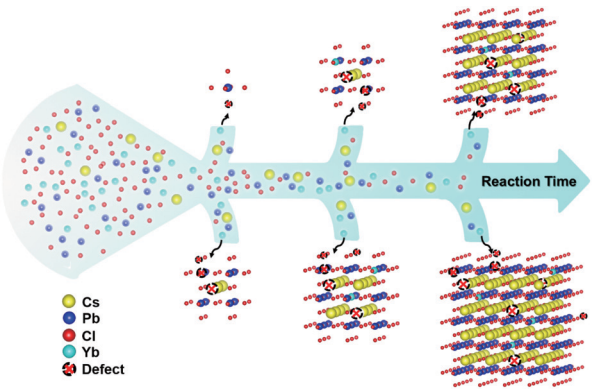

Fig. 10 Schematic illustration of the proposed growth process of doped $CsPbCl_3$ NCs.

Models for the defect-assisted doping efficiency

We note that macroscopic semiconductors grown under thermal equilibrium can be doped with foreign ions up to their solid solubility limit, which is completely determined by the Gibbs free energy and the growth temperature.[51] However, colloidal NCs, not limited to $CsPbX_3$ studied here, are typically grown using colloidal synthesis at much lower temperatures, which corresponds to growth conditions featuring thermal non-equilibrium. Therefore, the incorporation of dopants into NCs can be viewed as a kinetic process that is intimately associated with adsorption of dopant ions during growth of NCs.[51] Based on these facts, a possible mechanism for the defect-assisted doping is thus proposed as follows. Given the characteristics of colloidal synthesis, the structural defects (*e.g.*, atomic vacancies, vacancy complexes) could be randomly and unintentionally introduced into the lattices of some NCs during the one-pot growth, which causes the difference in the defect amount at different growth stages for different NCs (Fig. 10). From this perspective, it becomes understandable that the formation of a higher-concentration of atomic point defects during assembly of the constituent atoms should provide more channels for adsorption and then incorporation of dopant ions, resulting in a larger doping efficiency (Fig. 10). One possible source for the formation of defects can be connected with a fast growth rate, which may cause imperfect assembly of constituent atoms, as experimentally found in undoped NCs (Fig. S9, ESI†). Another possible source may be due to the dopant-related structural defects formed during growth of NCs, which may further trigger the adsorption and then incorporation of dopants. Additionally, intentional tuning of growth conditions that favor the occurrence of deficiencies of constituent atoms can also enhance the doping efficiency of the targeted system (Fig. S14, ESI†). We underscore that our finding suggests that structural defects can play a positive role in enhancing the doping efficiency of lanthanide-doped lead halide perovskite NCs, which does not rule out other possibilities to tune the doping efficiency by tailoring the synthesis parameters.

Conclusions

To summarize, we have systematically investigated the local structure of dopants, doping efficiency, and luminescence properties of lanthanide-doped lead halide perovskite NCs. By using Yb^{3+}-doped $CsPbCl_3$ NCs as a model system, we showed that the Yb^{3+} ions occupy the Pb^{2+} crystallographic sites in $CsPbCl_3$ NCs. Our work presents the first experimental evidence that rare earth ions can be heterovalently incorporated into the perovskite lattice. On the basis of the combined experimental and theoretical evidence, we identified that structural defects formed during growth of halide perovskite NCs play a positive role in enhancing the doping efficiency of the NCs, *i.e.*, that the formation of a higher-concentration of defects facilitates the introduction of a higher-concentration of dopant ions. We demonstrated that the concept of defect-assisted doping can be adopted as a guideline to rationally tune the doping efficiency of lanthanide-doped halide perovskite NCs. We also found that lanthanide-doped $CsPbCl_3$ NCs can exhibit anomalous photophysical behaviors of the band-edge emission, which we propose is due to the existence of shallow trapping states near the conduction band. This work establishes the relationship between structural defects and doping efficiency in lanthanide-doped halide perovskite NCs, and suggests the possibility of doping previously undopable ions into halide perovskite lattices by intentionally creating structural defects. We think that these insights present a model case for understanding the local structure of dopants, doping efficiency, and luminescence properties of doped halide perovskite polycrystalline films and other families of NCs.

Author contributions

H.-T. Sun conceived the research. J.-P. Ma, Y.-M. Chen, and L.-M. Zhang performed most of the experiments and data analysis. J.-Y. Zhang and S.-Q. Guo performed the DFT calculations. Jian-Dang Liu, Bang-Jiao Ye, and Hong Li took the positron annihilation lifetime spectra. Z.-Y. Li, Y. Zhou, and B.-B. Zhang made the EXAFS measurements. O. M. Bakr and H.-T. Sun analyzed the temperature-dependent luminescence spectra. H.-T. Sun and J.-Y. Zhang supervised the research. J.-P. Ma and H.-T. S. wrote the manuscript with input from the other authors. All the authors discussed the results and commented on the manuscript.

Conflicts of interest

The authors declare no competing financial interests.

Acknowledgements

This work was supported by the National Natural Science Foundation of China (Grant No. 11874275, 11574225, and 51672106), and two projects funded by the Priority Academic Program Development of Jiangsu Higher Education Institutions (PAPD) and State Key Laboratory of Luminescence and Applications, Chinese Academy of Sciences (Grant No. SKLA-2018-04). This work was carried out at National Supercomputer Center in Tianjin, and the calculations were performed on TianHe-1(A).

Notes and references

1 L. Protesescu, S. Yakunin, M. I. Bodnarchuk, F. Krieg, R. Caputo, C. H. Hendon, R. X. Yang, A. Walsh and M. V. Kovalenko, *Nano Lett.*, 2015, **15**, 3692–3696.
2 S. Yakunin, L. Protesescu, F. Krieg, M. I. Bodnarchuk, G. Nedelcu, M. Humer, G. De Luca, M. Fiebig, W. Heiss and M. V. Kovalenko, *Nat. Commun.*, 2015, **6**, 8056.
3 L. C. Schmidt, A. Pertegás, S. González-Carrero, O. Malinkiewicz, S. Agouram, G. Minguez Espallargas, H. J. Bolink, R. E. Galian and J. Pérez-Prieto, *J. Am. Chem. Soc.*, 2014, **136**, 850–853.
4 Q. A. Akkerman, M. Gandini, F. Di Stasio, P. Rastogi, F. Palazon, G. Bertoni, J. M. Ball, M. Prato, A. Petrozza and L. Manna, *Nat. Energy*, 2016, **2**, 16194.
5 J. Z. Song, J. H. Li, X. M. Li, L. M. Xu, Y. H. Dong and H. B. Zeng, *Adv. Mater.*, 2015, **27**, 7162–7167.
6 Q. A. Akkerman, S. G. Motti, A. R. Srimath Kandada, E. Mosconi, V. D'Innocenzo, G. Bertoni, S. Marras, B. A. Kamino, L. Miranda, F. De Angelis, A. Petrozza, M. Prato and L. Manna, *J. Am. Chem. Soc.*, 2016, **138**, 1010–1016.
7 H. Huang, L. Polavarapu, J. A. Sichert, A. S. Susha, A. S. Urban and A. L. Rogach, *NPG Asia Mater.*, 2016, **8**, e328.
8 G. Rainò, G. Nedelcu, L. Protesescu, M. I. Bodnarchuk, M. V. Kovalenko, R. F. Mahrt and T. Stöferle, *ACS Nano*, 2016, **10**, 2485–2490.
9 Z. C. Li, L. Kong, S. Q. Huang and L. Li, *Angew. Chem., Int. Ed.*, 2017, **56**, 8134–8138.
10 F. Liu, Y. H. Zhang, C. Ding, S. Kobayashi, T. Izuishi, N. Nakazawa, T. Toyoda, T. Ohta, S. Hayase, T. Minemoto, K. Yoshino, S. Y. Dai and Q. Shen, *ACS Nano*, 2017, **11**, 10373–10383.
11 E. M. Sanehira, A. R. Marshall, J. A. Christians, S. P. Harvey, P. N. Ciesielski, L. M. Wheeler, P. Schulz, L. Y. Lin, M. C. Beard and J. M. Luther, *Sci. Adv.*, 2017, **3**, eaao4204.
12 H. Huang, Q. Xue, B. K. Chen, Y. Xiong, J. Schneider, C. Y. Zhi, H. Z. Zhong and A. L. Rogach, *Angew. Chem., Int. Ed.*, 2017, **56**, 9571–9576.
13 S. Ghosh and L. Manna, *Chem. Rev.*, 2018, **118**, 7804–7864.
14 M. Imran, V. Caligiuri, M. Wang, L. Goldoni, M. Prato, R. Krahne, L. De Trizio and L. Manna, *J. Am. Chem. Soc.*, 2018, **140**, 2656–2664.
15 S. Muduli, P. Pandey, G. Devatha, R. Babar, M. Thripuranthaka, D. C. Kothari, M. Kabir, P. P. Pillai and S. Ogale, *Angew. Chem., Int. Ed.*, 2018, **57**, 7682–7686.
16 W. Zheng, P. Huang, Z. L. Gong, D. Tu, J. Xu, Q. L. Zou, R. F. Li, W. W. You, J. G. Bünzli and X. Y. Chen, *Nat. Commun.*, 2018, **9**, 3462.
17 N. J. Jeon, J. H. Noh, W. S. Yang, Y. C. Kim, S. Ryu, J. Seo and S. I. Seok, *Nature*, 2015, **517**, 476–480.

18 D. P. McMeekin, G. Sadoughi, W. Rehman, G. E. Eperon, M. Saliba, M. T. Hörantner, A. Haghighirad, N. Sakai, L. Korte and B. Rech, *Science*, 2016, **351**, 151–155.
19 R. S. Sanchez, M. S. de la Fuente, I. Suarez, G. Muñoz-Matutano, J. P. Martinez-Pastor and I. Mora-Sero, *Sci. Adv.*, 2016, **2**, e1501104.
20 B. R. Sutherland and E. H. Sargent, *Nat. Photonics*, 2016, **10**, 295–302.
21 Y. Tong, E. Bladt, M. F. Aygüler, A. Manzi, K. Z. Milowska, V. A. Hintermayr, P. Docampo, S. Bals, A. S. Urban, L. Polavarapu and J. Feldmann, *Angew. Chem., Int. Ed.*, 2016, **55**, 13887–13892.
22 M. V. Kovalenko, L. Protesescu and M. I. Bodnarchuk, *Science*, 2017, **358**, 745–750.
23 Y. Zhou, J. Chen, O. M. Bakr and H.-T. Sun, *Chem. Mater.*, 2018, **30**, 6589–6613.
24 A. L. Abdelhady, M. I. Saidaminov, B. Murali, V. Adinolfi, O. Voznyy, K. Katsiev, E. Alarousu, R. Comin, I. Dursun, L. Sinatra, E. H. Sargent, O. F. Mohammed and O. M. Bakr, *J. Phys. Chem. Lett.*, 2016, **7**, 295–301.
25 Y. Zhou, Z. J. Yong, K. C. Zhang, B. M. Liu, Z. W. Wang, J. S. Hou, Y. Z. Fang, Y. Zhou, H. T. Sun and B. Song, *J. Phys. Chem. Lett.*, 2016, **7**, 2735–2741.
26 R. Begum, M. R. Parida, A. L. Abdelhady, B. Murali, N. M. Alyami, G. H. Ahmed, M. N. Hedhili, O. M. Bakr and O. F. Mohammed, *J. Am. Chem. Soc.*, 2017, **139**, 731–737.
27 D. Parobek, B. J. Roman, Y. Dong, H. Jin, E. Lee, M. Sheldon and D. H. Son, *Nano Lett.*, 2016, **16**, 7376–7380.
28 W. Y. Liu, Q. L. Lin, H. B. Li, K. F. Wu, I. Robel, J. M. Pietryga and V. I. Klimov, *J. Am. Chem. Soc.*, 2016, **138**, 14954–14961.
29 G. G. Huang, C. L. Wang, S. H. Xu, S. F. Zong, J. Lu, Z. Y. Wang, C. G. Lu and Y. P. Cui, *Adv. Mater.*, 2017, **29**, 1700095.
30 S. Das Adhikari, S. K. Dutta, A. Dutta, A. K. Guria and N. Pradhan, *Angew. Chem., Int. Ed.*, 2017, **56**, 8746–8750.
31 H. W. Liu, Z. N. Wu, J. R. Shao, D. Yao, H. Gao, Y. Liu, W. L. Yu, H. Zhang and B. Yang, *ACS Nano*, 2017, **11**, 2239–2247.
32 K. Y. Xu, C. C. Lin, X. B. Xie and A. Meijerink, *Chem. Mater.*, 2017, **29**, 4265–4272.
33 D. Parobek, Y. T. Dong, T. Qiao and D. H. Son, *Chem. Mater.*, 2018, **30**, 2939–2944.
34 Z.-J. Yong, S.-Q. Guo, J.-P. Ma, J.-Y. Zhang, Z.-Y. Li, Y.-M. Chen, B.-B. Zhang, Y. Zhou, J. Shu and J.-L. Gu, *J. Am. Chem. Soc.*, 2018, **140**, 9942–9951.
35 F.-P. Zhu, Z.-J. Yong, B.-M. Liu, Y.-M. Chen, Y. Zhou, J.-P. Ma, H.-T. Sun and Y.-Z. Fang, *Opt. Express*, 2017, **25**, 33283–33289.
36 D. L. Zhou, D. L. Liu, G. C. Pan, X. Chen, D. Y. Li, W. Xu, X. Bai and H. W. Song, *Adv. Mater.*, 2017, **29**, 1704149.
37 G. C. Pan, X. Bai, D. W. Yang, X. Chen, P. T. Jing, S. G. Qu, L. J. Zhang, D. L. Zhou, J. Y. Zhu and W. Xu, *Nano Lett.*, 2017, **17**, 8005–8011.
38 T. J. Milstein, D. M. Kroupa and D. R. Gamelin, *Nano Lett.*, 2018, **18**, 3792–3799.
39 Q. S. Hu, Z. Li, Z. F. Tan, H. B. Song, C. Ge, G. D. Niu, J. T. Han and J. Tang, *Adv. Opt. Mater.*, 2018, **6**, 1700864.
40 W. J. Mir, Y. Mahor, A. Lohar, M. Jagadeeswararao, S. Das, S. Mahamuni and A. Nag, *Chem. Mater.*, 2018, **30**, 8170–8178.
41 X. Li, S. Duan, H. C. Liu, G. Y. Chen, Y. Luo and H. Agren, *J. Phys. Chem. Lett.*, 2019, **10**, 487–492.
42 X. Luo, T. Ding, X. Liu, Y. Liu and K. F. Wu, *Nano Lett.*, 2019, **19**, 338–341.
43 J. L. Duan, Y. Y. Zhao, X. Y. Yang, Y. Wang, B. L. He and Q. W. Tang, *Adv. Energy Mater.*, 2018, **8**, 1802346.
44 L. Zhou, T. R. Liu, J. Zheng, K. Yu, F. Yang, N. Wang, Y. H. Zuo, Z. Liu, C. L. Xue, C. B. Li, B. W. Cheng and Q. M. Wang, *J. Phys. Chem. C*, 2018, **122**, 26825–26834.
45 G. H. Ahmed, J. K. El-Demellawi, J. Yin, J. Pan, D. B. Velusamy, M. N. Hedhili, E. Alarousu, O. M. Bakr, H. N. Alshareef and O. F. Mohammed, *ACS Energy Lett.*, 2018, **3**, 2301–2307.
46 S. H. Zou, Y. S. Liu, J. H. Li, C. P. Liu, R. Feng, F. L. Jiang, Y. Li, J. Z. Song, H. B. Zeng and M. C. Hong, *J. Am. Chem. Soc.*, 2017, **139**, 11443–11450.
47 D. M. Kroupa, J. Y. Roh, T. J. Milstein, S. E. Creutz and D. R. Gamelin, *ACS Energy Lett.*, 2018, **3**, 2390–2395.
48 F. Zhang, H. Z. Zhong, C. Chen, X.-g. Wu, X. M. Hu, H. L. Huang, J. B. Han, B. S. Zou and Y. P. Dong, *ACS Nano*, 2015, **9**, 4533–4542.
49 M. C. Brennan, J. Zinna and M. Kuno, *ACS Energy Lett.*, 2017, **2**, 1487–1488.
50 M. Lorenzon, L. Sortino, Q. Akkerman, S. Accornero, J. Pedrini, M. Prato, V. Pinchetti, F. Meinardi, L. Manna and S. Brovelli, *Nano Lett.*, 2017, **17**, 3844–3853.
51 S. C. Erwin, L. Zu, M. I. Haftel, A. L. Efros, T. A. Kennedy and D. J. Norris, *Nature*, 2005, **436**, 91–94.
52 J. B. Miller, J. M. Harris and E. K. Hobbie, *Langmuir*, 2014, **30**, 7936–7946.
53 G. Kresse and J. Furthmüller, *Phys. Rev. B: Condens. Matter Mater. Phys.*, 1996, **54**, 11169–11186.
54 G. Kresse and D. Joubert, *Phys. Rev. B: Condens. Matter Mater. Phys.*, 1999, **59**, 1758–1778.
55 M. Ghebouli, B. Ghebouli and M. Fatmi, *Phys. B*, 2011, **406**, 1837–1843.
56 B. Ravel and M. Newville, *J. Synchrotron Radiat.*, 2005, **12**, 537–541.
57 M. A. Becker, R. Vaxenburg, G. Nedelcu, P. C. Sercel, A. Shabaev, M. J. Mehl, J. G. Michopoulos, S. G. Lambrakos, N. Bernstein, J. L. Lyons, T. Stoferle, R. F. Mahrt, M. V. Kovalenko, D. J. Norris, G. Raino and A. L. Efros, *Nature*, 2018, **553**, 189–193.
58 M. C. Brennan, J. E. Herr, T. S. Nguyen-Beck, J. Zinna, S. Draguta, S. Rouvimov, J. Parkhill and M. Kuno, *J. Am. Chem. Soc.*, 2017, **139**, 12201–12208.
59 F. Bertolotti, L. Protesescu, M. V. Kovalenko, S. Yakunin, A. Cervellino, S. J. Billinge, M. W. Terban, J. S. Pedersen, N. Masciocchi and A. Guagliardi, *ACS Nano*, 2017, **11**, 3819–3831.
60 B. M. Liu, Z. G. Zhang, K. Zhang, Y. Kuroiwa, C. Moriyoshi, H. M. Yu, C. Li, L. R. Zheng, L. N. Li, G. Yang, Y. Zhou,

Y. Z. Fang, J. S. Hou, Y. Matsushita and H. T. Sun, *Angew. Chem., Int. Ed.*, 2016, **55**, 4967–4971.

61 B. Lengeler and P. Eisenberger, *Phys. Rev. B: Condens. Matter Mater. Phys.*, 1980, **21**, 4507–4520.

62 Z. J. Li, E. Hofman, A. H. Davis, A. Khammang, J. T. Wright, B. Dzikovski, R. W. Meulenberg and W. W. Zheng, *Chem. Mater.*, 2018, **30**, 6400–6409.

63 M. Chakrabarti, D. Jana and D. Sanyal, *Vacuum*, 2013, **87**, 16–20.

64 X. C. Jiao, Z. W. Chen, X. D. Li, Y. F. Sun, S. Gao, W. S. Yan, C. M. Wang, Q. Zhang, Y. Lin and Y. Luo, *J. Am. Chem. Soc.*, 2017, **139**, 7586–7594.

65 J. Li, X. Y. Wu, W. F. Pan, G. K. Zhang and H. Chen, *Angew. Chem., Int. Ed.*, 2018, **57**, 491–495.

66 R. D. Shannon, *Acta Crystallogr., Sect. A: Cryst. Phys., Diffr., Theor. Gen. Crystallogr.*, 1976, **32**, 751–767.

67 N. Mondal, A. De and A. Samanta, *ACS Energy Lett.*, 2019, **4**, 32–39.

